

Article

Calcium Carbonate@silica Composite with Superhydrophobic Properties

Yitong Ma ¹, Pei Tian ¹, Malayphone Bounmyxay ¹, Yiwen Zeng ^{2,*} and Nong Wang ^{1,*} 

¹ School of Chemistry and Chemical Engineering, Lanzhou Jiaotong University, Lanzhou 730070, China; mayitong0822@163.com (Y.M.); tienpei_977@163.com (P.T.); jingxiaolian012@163.com (M.B.)

² Guangxi Key Laboratory of Calcium Carbonate Resources Comprehensive Utilization, College of Materials and Chemical Engineering, Hezhou University, Hezhou 542899, China

* Correspondence: 13481457176@126.com (Y.Z.); wangn@mail.lzjtu.cn (N.W.)

Abstract: In this paper, spherical calcium carbonate particles were prepared by using CaCl₂ aqueous solution + NH₃·H₂O + polyoxyethylene octyl phenol ether-10 (OP-10) + n-butyl alcohol + cyclohexane inverse micro emulsion system. Then, nanoscale spherical silica was deposited on the surface of micron calcium carbonate by Stöber method to form the composite material. Scanning electron microscope (SEM), X-ray powder diffraction (XRD), Fourier transform infrared spectroscopy (FTIR), Thermogravimetric analysis (TGA) and X-ray photoelectron spectroscopy (XPS) were used to characterize the morphology and structure of the composite material. It is found that the surface of the composite material has a micro-nano complex structure similar to the surface of a “lotus leaf”, making the composite material show hydrophobicity. The contact angle of the cubic calcium carbonate, spherical calcium carbonate and CaCO₃@SiO₂ composite material were measured. They were 51.6°, 73.5°, and 76.8°, respectively. After modification with stearic acid, the contact angle of cubic and spherical CaCO₃ were 127.1° and 136.1°, respectively, while the contact angle of CaCO₃@SiO₂ composite was 151.3°. These results showed that CaCO₃@SiO₂ composite had good superhydrophobicity, and the influence of material roughness on its hydrophobicity was investigated using the Cassie model theory.

Keywords: composite material; roughness; hydrophobicity; contact angle



Citation: Ma, Y.; Tian, P.; Bounmyxay, M.; Zeng, Y.; Wang, N. Calcium Carbonate@silica Composite with Superhydrophobic Properties. *Molecules* **2021**, *26*, 7180. <https://doi.org/10.3390/molecules26237180>

Academic Editor:
Piersandro Pallavicini

Received: 3 November 2021
Accepted: 24 November 2021
Published: 26 November 2021

Publisher's Note: MDPI stays neutral with regard to jurisdictional claims in published maps and institutional affiliations.



Copyright: © 2021 by the authors. Licensee MDPI, Basel, Switzerland. This article is an open access article distributed under the terms and conditions of the Creative Commons Attribution (CC BY) license (<https://creativecommons.org/licenses/by/4.0/>).

1. Introduction

Over thousands of years of natural selection, living organisms, including all plants and animals on our earth, have become evolutionarily optimized functional systems. One of their most fascinating properties is their ability of self-cleaning, which means that their surfaces can repel contaminants such as solid particles, organic liquids, and biological contaminants by the action of rolling-off water drops. Due to the lotus leaf being used as the typical representative, this kind of hydrophobicity or self-cleaning property has been known as the “lotus effect” [1–8]. In 1998, after Barthlott described lotus leaf self-cleaning behavior, the lotus leaf effect attracted wide attention in the study of biological surfaces, and many researchers focused on the preparation of various self-cleaning materials [9–11].

The contact and sliding angle of a drop are a quantitative measure of self-cleaning behavior. It is considered that both hydrophobicity and low contact angle hysteresis are necessary for self-cleaning surfaces [12–14]. The contact angle hysteresis is also related to the roughness and surface tension of the material. In general, in order to make a superhydrophobic surface (water contact angle > 150°), the nanometer scale roughness and hydrophobic surface (smooth surface contact angle > 90°) are two basic requirements [15].

Calcium carbonate is a kind of important inorganic chemical raw materials. Due to its many advantages such as a rich material source, simple working process, high product quality, low cost, etc., micro and nano calcium carbonate powder have been widely used in the paper making [16,17], paint, rubber [18], and adhesives industry [19]. In addition,

due to their good stability, biocompatibility and biodegradability, calcium carbonate can be used as drug or gene carrier in biomedical fields and substrate for the manufacturing of mixed materials with different functions [20,21].

The finer the surface of calcium carbonate, the higher the surface energy and the easier it is to self-agglomerate in polar solvents. Its surface is hydrophilic and oleophobic, and it is therefore not easy to bind to organisms with low surface energy and it is difficult to disperse in polymers. By modifying the surface of calcium carbonate powder, its surface energy can be reduced, its dispersibility can be improved, and its surface can be changed from hydrophilic to hydrophobic [22].

As a kind of multifunctional material, silica is used in many fields, such as in microelectronic devices, optical fiber, and can also be used as a chromatographic column packing and catalyst carrier [23–25]. Because its properties are very stable and its surface can be modified easily with appropriate heat treatment or chemical treatment, which are responsible for the physical and chemical properties of silica, it thus makes these materials very attractive for academic research and technical applications [26–31]. Nano-silica is the most widely used inorganic nonmetallic nanomaterials at present. There are different bonded hydroxyl groups on the surface of nano-silica, which mainly have three forms: (1) isolated silanols, (2) vicinal silanols, and (3) geminal silanols. These groups have strong water absorption and are prone to agglomeration [32].

Composite materials are composed of two or more materials with different properties by physical or chemical methods, which have a series of excellent characteristics, such as good bearing capacity, excellent mechanical properties, strong vibration reduction, wear resistance, heat resistance, and material design, etc. Various materials have complementary and synergistic effects in performance, so that the composite material's comprehensive properties are better than the original constituent materials and meet different requirements [33–35]. So, if the nano scale silica is deposited with calcium carbonate surface to form a composite material, the overall roughness of the material can be increased [36].

The reversed-phase microemulsion method is a new material preparation method developed in recent years [37,38]. It is an oil-in-water (or water-in-oil) dispersion system composed of an oil phase, water phase, and a surfactant. The tiny "pool" in the inverting microemulsion is surrounded by a monolayer composed of surfactants and co-surfactants. Because of the special properties of the surfactant, the size of the "pool" can be controlled by adjusting the molar ratio of the surfactant. At present, the method of preparing nano-materials using microemulsion as the template has been widely used in the preparation of composite catalysts, semiconductors, super-conductors, and magnetic nanoparticles [39,40]. This method of preparing micron or nano materials is easy to operate and does not need high temperature calcination. The size can be adjusted by changing its composition [41].

The wettability of a solid surface can be expressed by the contact angle (θ) of water droplets on the solid surface. If $90^\circ < \theta < 150^\circ$, the water droplets cannot easily infiltrate the solid surface, indicating that the solid surface is hydrophobic. If $\theta > 150^\circ$, the water droplets cannot infiltrate the solid surface, indicating that the solid surface is superhydrophobic. The free energy of the solid surface and the microstructure determine the wettability simultaneously [42].

As shown in Figure 1, the contact angle θ of liquid droplets on the solid surface is the angle between the solid-liquid interface and the tangent line of gas-liquid interface from the intersection point of gas liquid solid three phase [43]. Young's equation is the relationship between the free energies of solid-gas, solid-liquid, and liquid-gas interfaces γ_{sv} , γ_{sl} , γ_{lv} and the contact angle θ , which is also known as the wetting equation, and is expressed as:

$$\gamma_{sv} - \gamma_{sl} = \gamma_{lv} \cos\theta. \quad (1)$$

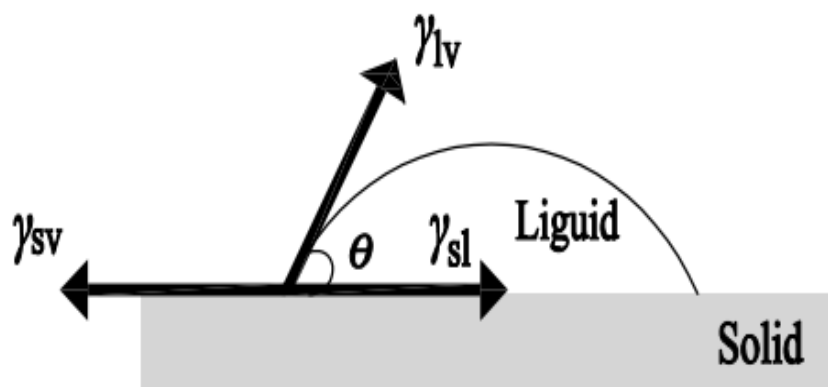


Figure 1. Standard vapor-solid-liquid three-phase interface.

Cassie believed that the contact of liquid drops on the rough surface was a kind of composite contact. Droplets on the hydrophobic surface could not fill the grooves on the rough surface, and there was trapped air under the droplet in the grooves. Therefore, the apparent solid-liquid contact was actually composed of solid-liquid and solid-gas contact. From the perspective of thermodynamics, at equilibrium, the apparent contact angle of the rough surface θ_r has the following relationship with the intrinsic contact angle of smooth surface θ_s :

$$\cos\theta_r = f(1 + \cos\theta_s) - 1, \quad (2)$$

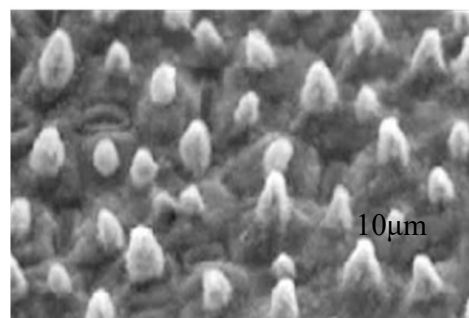
where f is the ratio of the apparent contact area to the raised solid area in the composite contact surface ($f < 1$). $r = 1/f$ is defined as the roughness of the material surface. So, the Cassie equation has the following relationship [44,45]:

$$\cos\theta_r = [(1 + \cos\theta_s)/r] - 1. \quad (3)$$

According to the electron microscope image, a large number of micron-sized waxy micropapillae are distributed on the surface of lotus leaves, and a large number of nanoscale bulge structures are distributed on each micropapillae, as shown in the Figure 2 [46]. Such micron-nano composite structure results in a low contact area and a large contact angle between water droplets and the surface of the lotus leaf.



(a)



(b)

Figure 2. (a) Typical digital photographs of superhydrophobic lotus leaf and water droplet on the lotus leaf. (b) Low magnification scanning electron microscope (SEM) image of the surface structures on the lotus leaf.

In this paper, composites similar to the surface structure of lotus leaves were prepared, and the influence of surface roughness on hydrophobicity was studied. Micron-sized spherical calcium carbonate was prepared by W/O microemulsion system with polyoxyethylene octyl phenol ether-10 (OP-10) as the surfactant [47,48], n-butanol as the co-surfactant,

and cyclohexane as the oil phase. Nano spherical silica was prepared by the Stöber method [49–51], which was loaded on micron-sized spherical calcium carbonate. After being modified by stearic acid, the coating prepared with the composite material resembled the “lotus effect”.

2. Materials and Methods

2.1. Materials

A total of 25% ammonia solution and calcium chloride were supplied by Tianjin Damao Chemical Factory, China. OP-10 and cyclohexane was provided by Shandong Shuangshuang Chemical Factory, China. N-butyl alcohol were purchased from Shanghai Ron reagent, China. Tetraethyl orthosilicate (TEOS) and n-hexane were purchased from Shanghai Zhongqin Chemical reagent, China. Stearic acid and isooctyl tetraethoxy silane (ITES) were supplied by Laiyang Chemical Factory, Laiyang, China. Distilled water was produced by our laboratory and was applied for all reactions and treatment processes. All the chemicals were analytical grade and used without further purification.

2.2. Preparation Method

Spherical calcium carbonate: 0.5 mol/L calcium chloride aqueous solution was prepared with ammonia water and calcium chloride. Then, we mixed the aqueous solution, cyclohexane, n-butyl alcohol, and OP-10 to prepare a stable inverse microemulsion. The volume ratio of the surfactant, co-surfactant, oil phase, and water phase were 15:15:50:4. The CO₂ gas was introduced into the microemulsion at the rate of 300 mL/min. With the continuous penetration of CO₂, the microemulsion began to become turbid, and micron scale spherical calcium carbonate was formed. During the precipitation, the solution was continuously stirred at a constant rate of 650 r/min. The yield of the final product was 0.19 g.

CaCO₃@SiO₂ composite material: The nano scale silica was generated by TEOS, ethanol, and ammonia. A total of 500 µL TEOS was diluted by 2 mL ammonia and 5 mL ethanol. After stirring for 2 h, 250 µL of ITES was added to the organic moieties incorporation by condensation reaction of TEOS. It was mixed with the turbid micron scale spherical calcium carbonate solution mentioned above and stirred in a constant temperature shaker at 70 °C for 3 h. Then, it was dried in a vacuum drying oven at 100 °C for 24 h to ensure that the silica was successfully loaded on the calcium carbonate. Finally, it was immersed in n-hexane solution of stearic acid for 1 h and dried in an oven at 70 °C. The yield of the final product was 0.31 g.

Cubic calcium carbonate: As a contrast, the cubic calcium carbonate was prepared. A total of 50 mL 0.5 mol/L calcium chloride aqueous solution, 1.1 mL OP-10, and 9 mL ethyl alcohol were mixed, then we let the solution stand for at least 48 h in the air. Micron scale cubic calcium carbonate particles were formed. The yield of the final product was 2.3 g.

2.3. Surface Treatment

A total of 20 g of dry powder of the materials mentioned above were well dispersed in 45 mL 0.5 mol/L stearic acid n-hexane solution. The suspension was continually stirred for 0.5 h. Then, the mixture was oven-dried at 70 °C. A double pressure sensitive adhesive tape with one side sticking on a glass slice was used as the substrate. The modified materials were spread on the surface of the adhesive tape and gently pressed with a glass cover. After pressing, the glass was flushed with air under pressure to remove free materials. This process, including powder spreading, pressing, and air flushing were repeated several times until the adhesive tape was fully covered by material particles.

2.4. Equipment and Characterization

The size and morphology of the composite material powder samples were analyzed by scanning electron microscopy (SEM; JSM-6100, JEOL Ltd., Tokyo, Japan). Infrared spectroscopy was recorded by a Fourier transform infrared spectrometer (FTIR; EXUS-470, Nicolet, Tokyo, Japan). The crystal structure types were analyzed by powder X-

ray diffraction (XRD; RINT-1000, Rigaku, Tokyo, Japan). The stability was studied by thermogravimetric analysis (TGA; TGA55, American TA Instrument Company, Hialeah, FL, USA). The contact angle was measured by a video optical contact angle tester (CA; OCA25, Eastern-Dataphy, Germany). The elements of the material were further analyzed with X-ray photoelectron spectroscopy (XPS; AXIS Supra, Kratos, Manchester, UK). All the glassware and storage bottles were immersed in hydrochloric acid overnight, then rinsed thoroughly with distilled water.

3. Results and Discussion

3.1. Morphology

Figure 3 are the scanning electron microscope photos of different material types. Figure 3a,b shows the cubic calcium carbonate particles, Figure 3c,d shows the spherical calcium carbonate particles prepared by the reverse microemulsion method, Figure 3e,f shows the composite material obtained by depositing nanoscale spherical silica on the surface of micron calcium carbonate. It can be seen from Figure 3a,b that the surface of the cubic calcium carbonate is smooth without any bumps, while the spherical calcium carbonate in Figure 3c,d is slightly concave and convex. The surface roughness of the composite material in Figure 3e,f is greatly increased due to the overall surface heterogeneity caused by the presence of spherical silica.

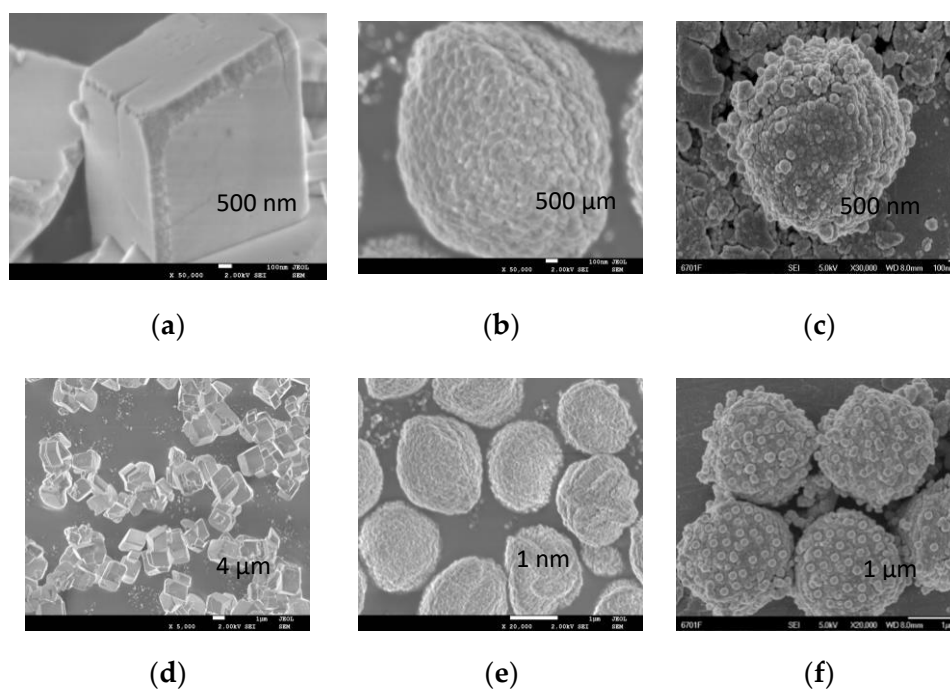


Figure 3. SEM image of cubic calcium carbonate (a,b), spherical calcium carbonate (c,d) and $\text{CaCO}_3@SiO_2$ composite material (e,f). $\text{CaCO}_3@SiO_2$ composite materials were formed by loading nanosized silica onto spherical calcium carbonate.

3.2. Structure and Crystal Type

Figure 4 shows the X-ray diffraction pattern of different material types. Vaterite and calcite are the two main crystal forms of calcium carbonate. The standard peaks of calcite crystal are consistent with the PDF#47-1743 [52]. It can be found that the diffraction peaks of cubic calcium carbonate (Figure 4a) appear at 2θ of 22.90° , 29.21° , 35.84° , 39.40° , 43.75° , 47.27° , and 48.94° . This is the same as the standard X-ray diffraction pattern for calcite, indicating that the prepared cubic micron calcium carbonate crystal form is mainly calcite. The diffraction peaks of spherical calcium carbonate (Figure 4b) appear at 20.81° , 24.72° , 26.93° , 29.35° , 32.60° , 43.83° , 48.92° , and 49.97° . The diffraction peaks at 20.8° , 24.7° , 26.9° , 32.6° , 43.8° , 48.9° , and 49.97° agree with the standard X-ray diffraction pattern

for vaterite [53], the diffraction peaks at 29.35° agree with the standard X-ray diffraction pattern for calcite, indicating that the spherical calcium carbonate mainly has vaterite [54]. Figure 4c shows the X-ray diffraction pattern of silica, the intense broad peak at $2\theta = 24^\circ$ represents the amorphous silica due to the smaller particle size effect and incomplete inner structure of the spherical nanoparticles [55]. Figure 4d shows the X-ray diffraction pattern of composite material. Compared to Figure 4b,c, Figure 4d can be considered as a superposition of the Figure 4b,c spectrum, indicating that the composite material is composed with a large amount of vaterite calcium carbonate, a small amount of calcite calcium carbonate, and some amorphous silica.

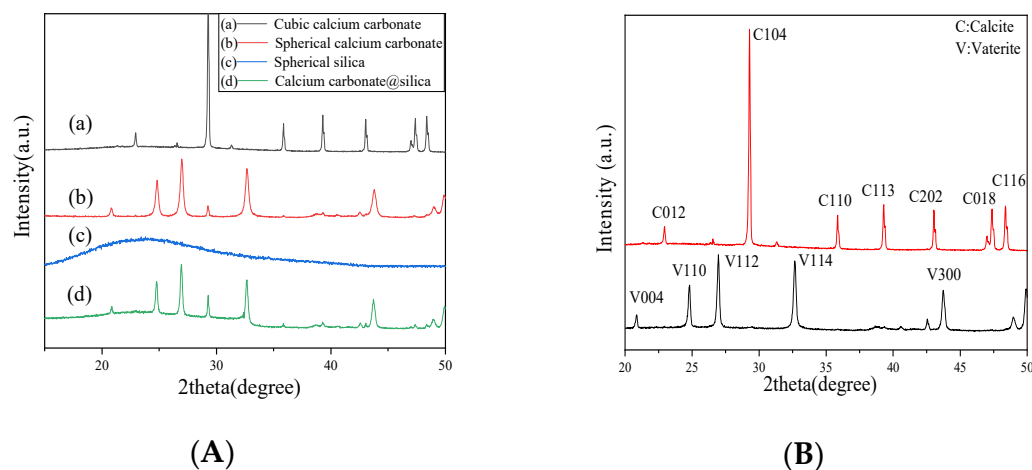


Figure 4. (A) X-ray diffraction pattern of different materials (a) cubic calcium carbonate, (b) spherical calcium carbonate, (c) spherical silica, and (d) $\text{CaCO}_3@\text{SiO}_2$ composite material. The black, red, blue, and green stick patterns in the XRD panels correspond to the (a), (b), (c), and (d). (B) The standard X-ray diffraction pattern of vaterite and calcite. The black and red stick patterns in the XRD panels correspond to the vaterite and calcite, respectively.

Figure 5 shows the infrared spectra of the cubic, spherical calcium carbonate and the composite material. The wavenumbers range change from 300 cm^{-1} to 2000 cm^{-1} . It can be seen that calcium carbonates (a) and (b) have absorption peaks at 1410 cm^{-1} , 1416 cm^{-1} , 873 cm^{-1} , 713 cm^{-1} , and 743 cm^{-1} , respectively. The absorption peaks at 1410 cm^{-1} and 1416 cm^{-1} are the C-O asymmetric stretching vibration [56]. The peak at 873 cm^{-1} is attributed to the out-of-plane bending vibration of the C-O bond [57]. For calcite and vaterite, the C-O asymmetric stretching vibration and out of plane bending vibrations, leading to the most intense peak, are at very similar positions, and thus cannot be used to distinguish between calcite and vaterite [58]. The peak at 713 cm^{-1} is attributed to the in-plane deformation vibration of the C-O bond of calcite crystal while the peak at 743 cm^{-1} is the characteristic absorption peaks of vaterite [59]. It can be seen that the composite material (c) has absorption peaks at 1416 cm^{-1} , 1082 cm^{-1} , 953 cm^{-1} , 873 cm^{-1} , 796 cm^{-1} , 744 cm^{-1} , and 458 cm^{-1} , respectively. The characteristic peak at 1082 cm^{-1} is attributed to the stretching symmetric vibrations of Si-O-Si. The peak at 953 cm^{-1} belongs to the asymmetric vibration absorption peak of Si-OH [60]. The peak at 796 cm^{-1} and 458 cm^{-1} is the symmetric stretching vibration and bending vibration of Si-O bond [61].

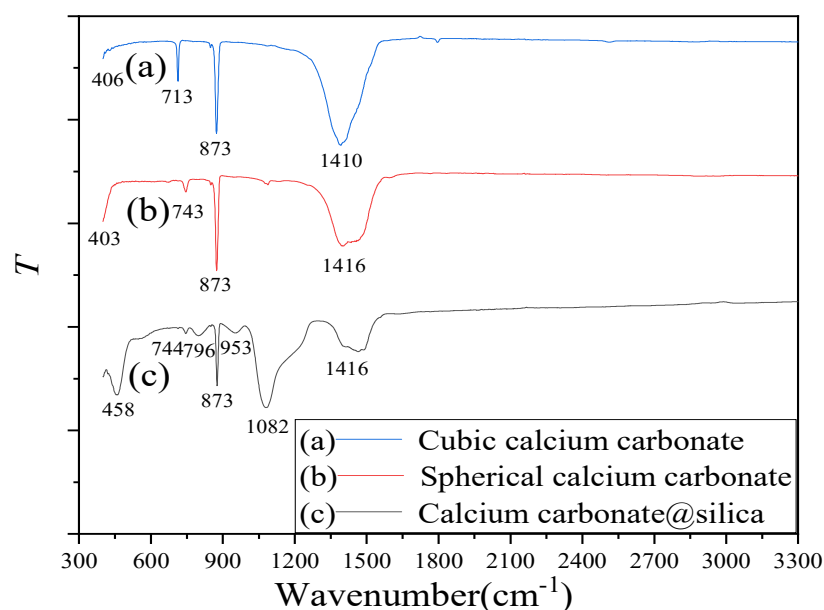


Figure 5. The FTIR of (a) cubic calcium carbonate, (b) spherical calcium carbonate, and (c) $\text{CaCO}_3@SiO_2$ composite material.

Thermogravimetry can be used to test the thermal stability of materials [62,63]. The TGA curves comparison between cubic calcium carbonate, spherical calcium carbonate and the composite material are shown in Figure 6. The weight loss of cubic and spherical calcium carbonate are mainly divided into two stages. The first region from room temperature $25\text{ }^\circ\text{C}$ to $610\text{ }^\circ\text{C}$ and the weight loss rate are about 2~4% and 3~5%. This is caused by intramolecular dehydration and carbonization of surfactants and cosurfactants adsorbed on the surface of calcium carbonate [64]. The weight loss rate is about 41.8~42.7% in the second region from temperature $610\text{ }^\circ\text{C}$ to $790\text{ }^\circ\text{C}$, which is attributed to the thermal decomposition of calcium carbonate into calcium oxide and CO_2 , while CO_2 escapes from the system. The weight loss of $\text{CaCO}_3@SiO_2$ is also mainly divided into two stages. At the first region of $25\text{ }^\circ\text{C}$ ~ $610\text{ }^\circ\text{C}$, the weight loss rate of $\text{CaCO}_3@SiO_2$ is about 5~6%, which is a little bit higher than cubic calcium carbonate and spherical calcium carbonate. This is because the composite material has a larger specific surface area, so it can adsorb more surfactants and cosurfactants, resulting in a larger weight loss rate of $\text{CaCO}_3@SiO_2$ in this stage. The second weight loss between $610\text{ }^\circ\text{C}$ and $790\text{ }^\circ\text{C}$ is due to part of the silica being undecomposed, so the weight loss rate is only about 34.8~35.7%.

Figure 7 shows the XPS characterization to verify that silica is loaded on the surface of the calcium carbonate. The peaks of O1s, Ca2p, C1s, and Si2p were shown by spectral scanning. The binding energies of C1s and O1s show characteristic peaks of the composite at 285.6 eV and 532.7 eV, respectively. The characteristic absorption peaks of Ca2p and Si2p appear at 347.5 eV and 101.5 eV, which correspond to the small figure in Figure 7, respectively [65]. The XPS spectrum of each element scan confirms that silica is successfully loaded on the surface of calcium carbonate.

3.3. Particle Size Analysis of Materials

Figure 8 shows the particle size analysis of the cubic, spherical calcium carbonate, and the composite material. The size and shape characterization of materials were based on SEM image analysis. The relevant length scale of cubic calcium carbonate is the side length. The spherical calcium carbonate and silica are approximately spherical and the relevant length scale is the diameter of spherical calcium carbonate and silica. In Figure 8c, the distribution of silica was shown on the left and the calcium carbonate was on the right. Nano measure software was used to analyze all images to obtain the mean values of length. Figure 8 shows the particle size distribution of materials. According to the particle

size distribution, cubic calcium carbonate has a diameter of about 1.55 μm . The diameter of spherical calcium carbonate is about 1.80 μm . In the composite, the diameter of the large sphere is about 2.05 μm and the diameter of the spherical crown is about 0.25 μm . The standard deviation calculated by standard deviation formula are ± 0.08 , ± 0.15 , and ± 0.25 , respectively, as shown in Table 1.

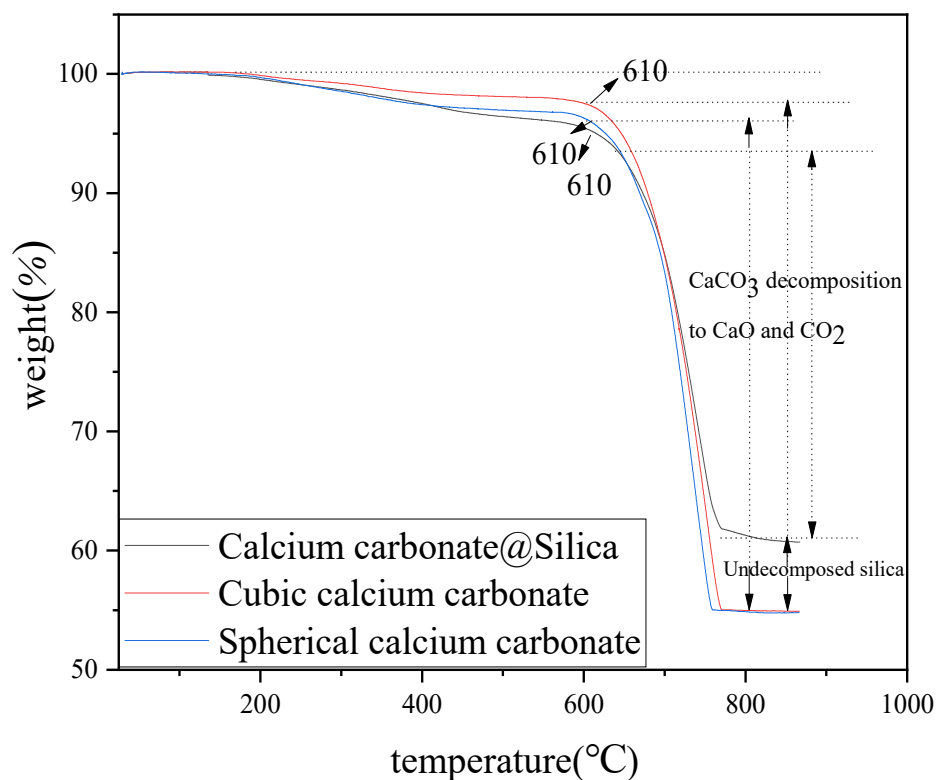


Figure 6. The TGA of $\text{CaCO}_3@SiO_2$ composite material and calcium carbonate. The temperature rises from 25 $^\circ\text{C}$ to 900 $^\circ\text{C}$.

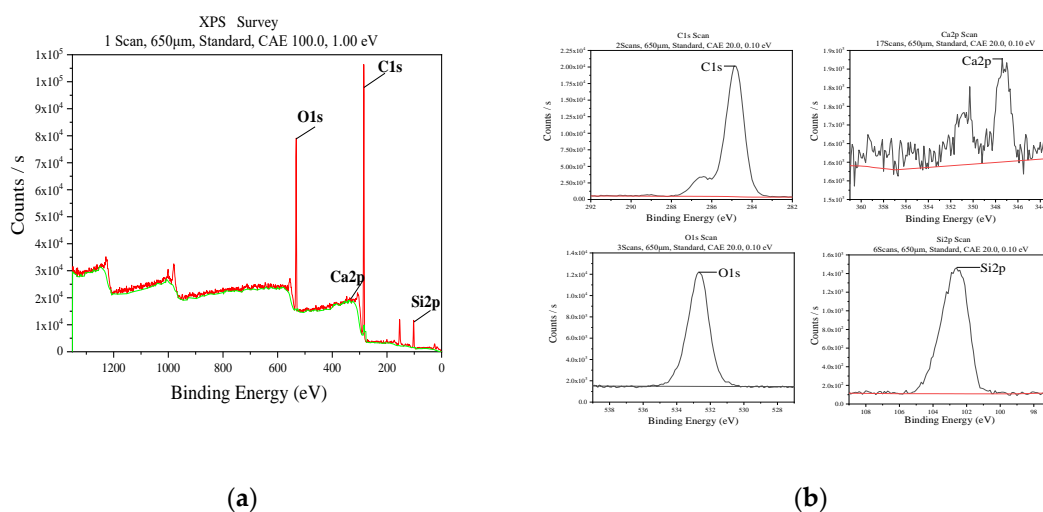


Figure 7. (a) The XPS spectra of $\text{CaCO}_3@SiO_2$ composite material. (b) The partial enlarged detail of (a).

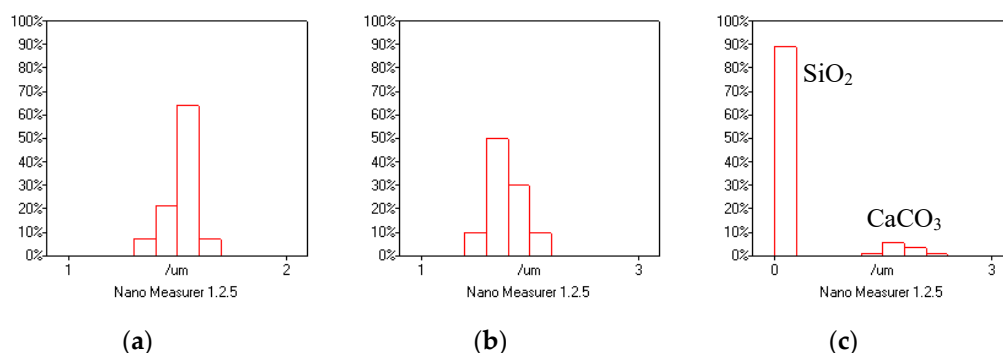


Figure 8. Particle size analysis of (a) cubic calcium carbonate, (b) spherical calcium carbonate, and (c) composite material.

Table 1. Average particle size and standard deviation of different materials.

	Cubic Calcium Carbonate	Spherical Calcium Carbonate	Composite Material
Mean value	1.55 μm	1.80 μm	2.05 μm
Standard deviation	± 0.08	± 0.15	± 0.25

3.4. Measurement of Hydrophobicity and Its Relationship with Roughness

Because the surface of $\text{CaCO}_3/\text{SiO}_2$ composite material and spherical calcium carbonate particles prepared in our lab were similar to the mastoid of lotus leaves surface due to the nano spherical silica adhere to the surface of the micron calcium carbonate, it will be interesting to see whether these materials will be superhydrophobic.

The hydrophobic performance was obtained by measuring the contact angle of water droplets on the surface of the materials [66,67]. The contact angles of the cubic calcium carbonate, spherical calcium carbonate and composite material are shown in Figure 9. The contact angle of cubic calcium carbonate, spherical calcium carbonate, and $\text{CaCO}_3/\text{SiO}_2$ composite material are 57.9° , 73.5° , and 76.8° , respectively.

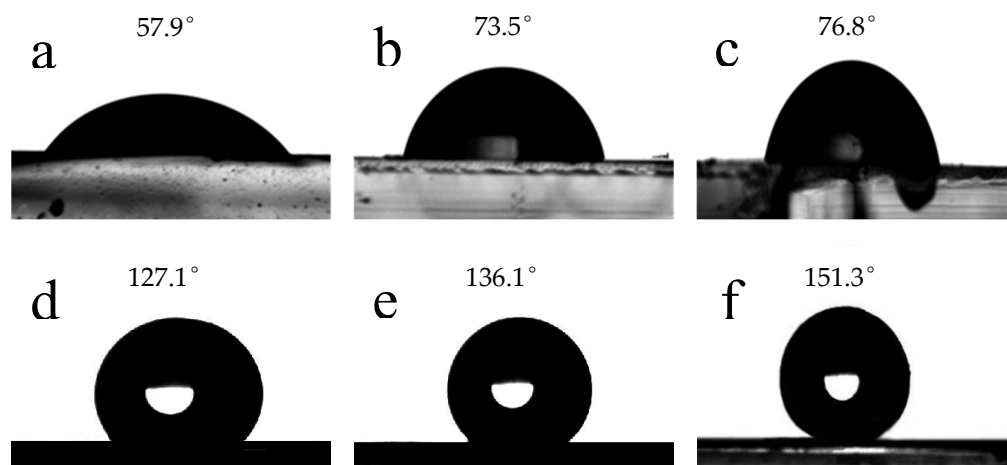


Figure 9. Contact angles of the materials coating on the glass. Unmodified: (a) Cubic calcium carbonate, (b) spherical calcium carbonate, (c) composite material. Modified by stearic acid: (d) cubic calcium carbonate, (e) spherical calcium carbonate, (f) composite material.

In addition, the “lotus leaf” effect is also due to the combined action of its surface wax composition and micron-nano composite structure, which endows the lotus leaf with its unique superhydrophobicity and self-cleaning ability. Therefore, the hydrophobicity of the cubic calcium carbonate, spherical calcium carbonate, and composite material were further

surface-treated by stearic acid, then made a coating on the glass. Their contact angles of the modified materials were measured. It can be seen from Figure 9d–f that the contact angles of the modified materials (θ_e) were 127.1° , 136.1° , and 151.3° , respectively. It was found that the hydrophobic performance of these materials was improved significantly after being modified by stearic acid, in particular, the composite material could achieve the purpose of superhydrophobic. Because the three different materials were all coated by stearic acid, the difference of hydrophobicity is mainly caused by the difference of their surface structure.

According to the Cassie model theory, the different roughness also has a certain different hydrophobicity. As can be seen from Figure 3, the surface of cubic calcium carbonate particles is relatively smooth, while the morphology of spherical calcium carbonate and composite material shows irregular spherical crowns. The size of the spherical crowns significantly impacts the roughness of the material, resulting in different hydrophobicity of the material.

As shown in Figure 10, spherical calcium carbonate and composite material can be regarded as micro spheres covered with nano spheres. The difference is that spherical calcium carbonate has less convex parts, while composite materials have more convex parts, which leads to the increase of roughness of materials. We assumed that the spherical crown of spherical calcium carbonate is $1/3$ height of the nano spherical CaCO_3 with a diameter of 60 nm, and the composite material is $2/3$ height of the nano spherical SiO_2 with a diameter of 400 nm. The specific surface area of spherical calcium carbonate and composite material can be calculated by calculating the area of the sphere crown. Because the surface of cubic calcium carbonate is flat, so it was used as a reference, according to the definition, the roughness r of the spherical calcium carbonate and $\text{CaCO}_3@/\text{SiO}_2$ composite material surfaces are their specific surface area divided by the specific surface area of cubic calcium carbonate.

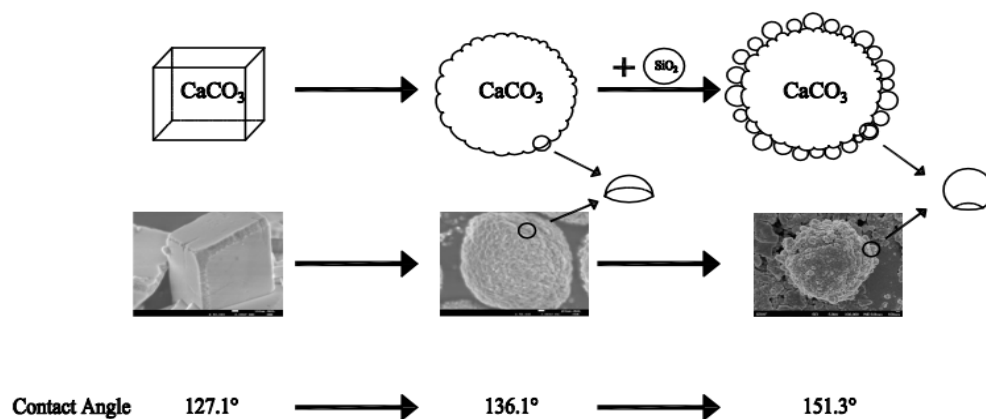


Figure 10. Calculation schematic diagram and experimental contact angle of different shapes of calcium carbonate. From cubic calcium carbonate to spherical calcium carbonate, then to composite material, the roughness of the materials is increasing.

Assuming that the roughness of cubic calcium carbonate surface is 1, the apparent contact angle θ_r of spherical calcium carbonate and composite material calculated by the Cassie equation is shown in Table 2. Meanwhile, the standard deviation of water contact angle is also added in Table 2. The superhydrophobic needle used for measurement is 0.51 mm outside diameter, 0.25 mm inside diameter, 38.1 mm in length, and the amount of water in each injection is $2 \mu\text{L}$ per time. According to experimental results, the superhydrophobicity of the composite is stable, and the standard deviations of experimental contact angle are less than 1° , as shown in Table 2. The error of the calculation results (θ_r) was also calculated from the error of the particle size, as shown in Table 2. From Table 2, we can also see that the results from calculation were consistent with those from experiment (θ_e). According to the calculation, the roughness has a significant impact on

the hydrophobicity, as the greater of the surface roughness, the better the hydrophobicity, which is consistent with the Cassie model. The material superhydrophobic can be modified by increasing the surface roughness.

Table 2. Comparison between experiment and theoretical calculation.

	Cubic Calcium Carbonate	Spherical Calcium Carbonate	Composite Material
Roughness (r)	1	1.3	2.3
Experimental results (θ_e)	$127.1^\circ \pm 0.85^\circ$	$136.1^\circ \pm 0.72^\circ$	$151.3^\circ \pm 0.76^\circ$
Calculation results (θ_r)	$127.1^\circ \pm 1.65^\circ$	$135.2^\circ \pm 2.20^\circ$	$150.1^\circ \pm 2.55^\circ$

4. Conclusions

In this paper, a new composite material of $\text{CaCO}_3@\text{SiO}_2$ was prepared by combining the nano structure with the micron structure, and the superhydrophobicity of the material was realized by increasing the surface roughness. The influence of the roughness on the hydrophobicity of the material was studied. It was found that after modification with stearic acid, the $\text{CaCO}_3@\text{SiO}_2$ composite had good superhydrophobicity, as the contact angle of $\text{CaCO}_3@\text{SiO}_2$ composite could reach 151.3° . Because all the composite materials were coated by stearic acid, their structure became the most important factor affecting hydrophobicity. The composite material we prepared achieves superhydrophobic performance due to the high roughness, which also provides a considerable prospect for us to prepare the superhydrophobic materials in the future. This study provides a new idea and method to study the superhydrophobic properties of rough surfaces by using the Cassie equation. The materials which we prepared are expected to be used as superhydrophobic coatings, for raincoats, waterproof glass, in the construction industry, and so on.

Author Contributions: Y.M. contributed to the syntheses, contact angle measurement and carried out the theoretical calculation, P.T. performed the TGA measurement, M.B. performed the IR measurement, Y.Z. performed SEM, N.W. designed the experiments, and all authors contributed to write the manuscript. All authors have read and agreed to the published version of the manuscript.

Funding: This research received no external funding.

Institutional Review Board Statement: Not applicable.

Informed Consent Statement: Not applicable.

Data Availability Statement: Not applicable.

Acknowledgments: This work was supported by the Key Technology and Industrial Application Demonstration Project of High Quality and High Purity Nano Calcium Carbonate of Guangxi Province (Grant No. 17202030-2), the Innovation Fund of Small and Medium-sized Enterprises of Gansu Province (Grant No. 1407GCCA013).

Conflicts of Interest: The authors declare that they have no conflict of interest.

Sample Availability: Not applicable.

References

1. Neinhuis, C.; Barthlott, W. Characterization and distribution of water-repellent, self-cleaning plant surfaces. *Ann. Bot.* **1997**, *79*, 667–677. [[CrossRef](#)]
2. Deng, D.; Lee, J.Y. Direct fabrication of double-rough chestnut-like multifunctional Sn@C composites on copper foil: Lotus effect and lithium ion storage properties. *J. Mater. Chem.* **2010**, *20*, 8045–8049. [[CrossRef](#)]
3. Frankiewicz, C.; Zoueshtiagh, F.; Talbi, A.; Streque, J.; Pernod, P.; Merlen, A. From ‘petal effect’ to ‘lotus effect’ on the highly flexible silastic elastomer microstructured using a fluorine based reactive ion etching process. *J. Micromech. Microeng.* **2014**, *24*, 1–9. [[CrossRef](#)]
4. Guo, Z.; Liu, W.; Su, B.-L. Superhydrophobic surfaces: From natural to biomimetic to functional. *J. Colloid Interface Sci.* **2011**, *353*, 335–355. [[CrossRef](#)] [[PubMed](#)]

5. Latthe, S.S.; Terashima, C.; Nakata, K.; Fujishima, A. Superhydrophobic surfaces developed by mimicking hierarchical surface morphology of Lotus Leaf. *Molecules* **2014**, *19*, 4256–4283. [[CrossRef](#)] [[PubMed](#)]
6. Nosonovsky, M.; Bhushan, B. Patterned nonadhesive surfaces: Superhydrophobicity and wetting regime transitions. *Langmuir* **2008**, *24*, 1525–1533. [[CrossRef](#)]
7. Barthlott, W.; Neinhuis, C. Purity of the sacred lotus, or escape from contamination in biological surfaces. *Planta* **1997**, *202*, 1–8. [[CrossRef](#)]
8. Zhang, M.; Feng, S.; Wang, L.; Zheng, Y. Lotus effect in wetting and self-cleaning. *Biotribology* **2016**, *5*, 31–43. [[CrossRef](#)]
9. Ebert, D.; Bhushan, B. Durable lotus-effect surfaces with hierarchical structure using micro- and nanosized hydrophobic silica particles. *J. Colloid Interface Sci.* **2012**, *368*, 584–591. [[CrossRef](#)]
10. Nun, E.; Oles, M.; Schleich, B. Lotus-effect-surfaces. *Macromol. Symp.* **2002**, *187*, 677–682. [[CrossRef](#)]
11. Spaeth, M.; Barthlott, W. Biomimetic super-hydrophobic surfaces and their application. *Adv. Sci. Technol.* **2008**, *60*, 38–46.
12. Spori, D.M.; Drobek, T.; Zürcher, S.; Ochsner, M.; Sprecher, C.; Mühlebach, A.; Spencer, N.D. Beyond the lotus effect: Roughness influences on wetting over a wide surface-energy range. *Langmuir* **2008**, *24*, 5411–5417. [[CrossRef](#)]
13. Bittoun, E.; Marmur, A. The role of multiscale roughness in the lotus effect: Is it essential for super-hydrophobicity? *Langmuir* **2012**, *28*, 13933–13942. [[CrossRef](#)]
14. Lee, H.J.; Michielsen, S. Lotus effect: Superhydrophobicity. *J. Text. Inst.* **2006**, *97*, 455–462. [[CrossRef](#)]
15. Hu, Z.; Deng, Y. Superhydrophobic surface fabricated from fatty acid-modified precipitated calcium carbonate. *Ind. Eng. Chem. Res.* **2010**, *49*, 5625–5630. [[CrossRef](#)]
16. Teofil, J.; Andrzej, K. Preparation of the hydrophilic/hydrophobic silica particles. *Colloids Surf. A Physicochem. Eng. Asp.* **2002**, *207*, 49–58.
17. Gaudreault, R.; Cesare, N.D.; Ven Theo, G.M.; Weitz, D.A. Structure and strength of flocs of precipitated calcium carbonate induced by various polymers used in papermaking. *Ind. Eng. Chem. Res.* **2015**, *54*, 6234–6246. [[CrossRef](#)]
18. Mori, Y.; Enomae, T.; Isogai, A. Application of vaterite-type calcium carbonate prepared by ultrasound for ink jet paper. *J. Imaging Sci. Technol.* **2010**, *54*, 1–6. [[CrossRef](#)]
19. Fang, Q.; Song, B.; Tee, T.-T.; Sin, L.T.; Hui, D.; Bee, S.-T. Investigation of dynamic characteristics of nano-size calcium carbonate added in natural rubber vulcanizate. *Compos. Part B Eng.* **2014**, *60*, 561–567. [[CrossRef](#)]
20. Atta, A.M.; Al-Lohedan, H.A.; Ezzat, A.O.; Al-Hussain, S.A. Characterization of superhydrophobic epoxy coatings embedded by modified calcium carbonate nanoparticles. *Prog. Org. Coat.* **2016**, *101*, 577–586. [[CrossRef](#)]
21. Ikoma, T.; Tonegawa, T.; Watanaba, H.; Chen, G.; Tanaka, J.; Mizushima, Y. Drug-supported microparticles of calcium carbonate nanocrystals and its covering with hydroxyapatite. *J. Nanosci. Nanotechnol.* **2007**, *7*, 822–827. [[CrossRef](#)]
22. Preisig, D.; Haid, D.; Varum, F.J.O.; Bravo, R.; Alles, R.; Huwyler, J. Drug loading into porous calcium carbonate microparticles by solvent evaporation. *Eur. J. Pharm. Biopharm.* **2014**, *87*, 548–558. [[CrossRef](#)]
23. Barrera, E.G.; Livotto, P.R.; Santos, J.H.Z. Hybrid silica bearing different organosilanes produced by the modified Stöber method. *Powder Technol.* **2016**, *301*, 486–492. [[CrossRef](#)]
24. Chen, H.; He, J. Rapid evaporation-induced synthesis of monodisperse budded silica spheres. *J. Colloid Interface Sci.* **2007**, *316*, 211–215. [[CrossRef](#)]
25. Hegde, N.D.; Rao, A.V. Organic modification of TEOS based silica aerogels using hexadecyltrimethoxysilane as a hydrophobic reagent. *Appl. Surf. Sci.* **2006**, *253*, 1566–1572. [[CrossRef](#)]
26. Larken, E.E.; Tina, M.T.; Timothy, J.D. Design of a doubly-hydrophilic block copolypeptide that directs the formation of calcium carbonate microspheres. *Chem. Commun.* **2004**, 1736–1737.
27. Pipatchanchai, T.; Srikulkit, K. Hydrophobicity modification of woven cotton fabric by hydrophobic fumed silica coating. *J. Sol.-Gel Sci. Technol.* **2007**, *44*, 119–123. [[CrossRef](#)]
28. Rezaei, S.; Manoucheri, I.; Moradian, R.; Pourabbas, B. One-step chemical vapor deposition and modification of silica nanoparticles at the lowest possible temperature and superhydrophobic surface fabrication. *Chem. Eng. J.* **2014**, *252*, 11–16. [[CrossRef](#)]
29. Trofimova, E.Y.; Kurdyukov, D.A.; Kukushkina, Y.A.; Yagovkina, M.A.; Golubev, V.G. Synthesis of monodispersed mesoporous spheres of submicron size amorphous silica. *Glass Phys. Chem.* **2011**, *37*, 378–384. [[CrossRef](#)]
30. Yao, L.; Xu, G.; Dou, W.; Bai, Y. The control of size and morphology of nanosized silica in Triton X-100 based reverse micelle. *Colloids Surf. A Physicochem. Eng. Asp.* **2008**, *316*, 8–14. [[CrossRef](#)]
31. Yong, W.Y.D.; Zhang, Z.; Cristobal, G.; Chin, W.S. One-pot synthesis of surface functionalized spherical silica particles. *Colloids Surf. A Physicochem. Eng. Asp.* **2014**, *460*, 151–157. [[CrossRef](#)]
32. Da, H.; Zhi, Y.; Xiaolin, L. Three-Dimensional Conductive Networks based on Stacked SiO₂@graphene Frameworks for Enhanced Gas Sensing. *Nanoscale* **2017**, 109–118.
33. Meng, H.; Zhao, T.; Jing, J.; Zeng, Y.; Wang, N. Preparation and properties of novel magnetic methylene blue molecularly imprinted polymer. *Polym. Sci. Ser. B* **2021**, *63*, 1–12.
34. Meng, H.; Zhao, T.; Wang, N. Adsorption and photodegradation properties of TiO₂-doped methylene blue molecular imprinted polymers. *Surf. Rev. Lett. (SRL)* **2021**, *28*, 1–12.
35. Sun, J.; Klechikov, A.; Moise, C.; Prodana, M.; Enachescu, M.; Talyzin, A.V. Molecular pillar approach to grow vertical covalent organic framework nanosheets on graphene: New hybrid materials for energy storage. *Angew. Chem.* **2017**, 1–7.

36. Maryam, K.; Sanaz, Z.G.; Sayed, A.A.A.; Kahila, B.; Mahdi, H.A.; Shayan, A. Recent Progress in the Study of Thermal Properties and Tribological Behaviors of Hexagonal Boron Nitride-Reinforced Composites. *J. Compos. Sci.* **2020**, *4*, 116.
37. Wang, N.; Wang, X.; Yang, L.; Chen, H. Morphology and size control of nanocalcium carbonate crystallised in reverse micelle system with cationic surfactant cetyltrimethylammonium bromide. *Micro Nano Lett.* **2013**, *8*, 94–98. [[CrossRef](#)]
38. Wang, N.; Yang, L.; Chen, L.; Xiao, R. Study of the influence between magnesium ions and calcium ions on the morphology and size of coprecipitation in microemulsion. *Micro Nano Lett.* **2014**, *9*, 302–307. [[CrossRef](#)]
39. Aramaki, K.; Hayashi, T.; Katsuragi, T.; Ishitobi, M.; Kunieda, H. Effect of adding an amphiphilic solubilization improver, sucrose distearate, on the solubilization capacity of nonionic microemulsions. *J. Colloid Interface Sci.* **2001**, *236*, 14–19. [[CrossRef](#)] [[PubMed](#)]
40. Liu, Y.; Chen, S.; Sheng, L.; Wang, M.; Liu, H. The phase behavior and solubilization ability of nonionic surfactant-distillate fraction of crude oil microemulsion system. *Colloids Surf. A Physicochem. Eng. Asp.* **2020**, *603*, 1–10. [[CrossRef](#)]
41. Maulvi, F.A.; Desai, A.R.; Choksi, H.H.; Patil, R.J.; Ranch, K.M.; Vyas, B.A.; Shah, D.O. Effect of surfactant chain length on drug release kinetics from microemulsion-laden contact lenses. *Int. J. Pharm.* **2017**, *524*, 193–204. [[CrossRef](#)]
42. Chen, W.; Alexander, Y.F.; Meng, C.H.; Jeffery, Y. Ultrahydrophobic and Ultralyophobic Surfaces: Some Comments and Examples. *Langmuir* **1999**, *15*, 3395–3399. [[CrossRef](#)]
43. Kwok, D.Y.; Neumann, A.W. Contact angle measurement and contact angle interpretation. *Adv. Colloid Interface Sci.* **1999**, *3*, 167–249. [[CrossRef](#)]
44. Cassie, A.B.D.; Baxter, S. Wettability of porous surfaces. *Trans. Faraday Soc.* **1944**, *40*, 546. [[CrossRef](#)]
45. Cassie, A.B.D. Contact angles. *Discuss. Faraday Soc.* **1948**, *3*, 11–16. [[CrossRef](#)]
46. Zorba, V.; Stratakis, E.; Barberoglou, M.; Spanakis, E.; Tzanetakis, P.; Anastasiadis, S.H.; Fotakis, C. Biomimetic artificial surfaces quantitatively reproduce the water repellency of a lotus leaf. *Adv. Mater.* **2008**, *21*, 4049–4054. [[CrossRef](#)]
47. Wang, N.; Lin, H.; Zhu, H. Study of the association behavior between bromophenol blue and octylphenol polyoxyethylene ether (10) in aqueous solution and the solubilization of bromophenol blue by micelles. *J. Solut. Chem.* **2016**, *45*, 1689–1700. [[CrossRef](#)]
48. Wang, N.; Zhao, M. Study on thermodynamics and kinetics of association interactions between malachite green and OP-10 in aqueous solutions. *J. Dispers. Sci. Technol.* **2015**, *37*, 190–195. [[CrossRef](#)]
49. Kobayashi, Y.; Katakami, H.; Mine, E.; Nagao, D.; Konno, M.; Liz-Marzán, L.M. Silica coating of silver nanoparticles using a modified Stöber method. *J. Colloid Interface Sci.* **2005**, *283*, 392–396. [[CrossRef](#)] [[PubMed](#)]
50. Larismaa, J.; Honkanen, T.; Ge, Y.; Söderberg, O.; Friman, M.; Hannula, S.-P. Effect of annealing on Ag-doped submicron silica powder prepared with modified stöber method. *Mater. Sci. Forum* **2011**, *695*, 449–452. [[CrossRef](#)]
51. Lei, X.; Yu, B.; Cong, H.-L.; Tian, C.; Wang, Y.-Z.; Wang, Q.-B.; Liu, C.-K. Synthesis of monodisperse silica microspheres by a modified stöber method. *Integr. Ferroelectr.* **2014**, *154*, 142–146. [[CrossRef](#)]
52. Wang, Y.; Lu, D. Study on oral ulcer powder using temperature-dependent X-ray diffraction technique. *Top. Chem. Mater. Eng.* **2018**, *1*, 104–106.
53. Kamhi, S.R. On the structure of vaterite CaCO₃. *Acta Crystallogr.* **1963**, *16*, 770–772. [[CrossRef](#)]
54. Lai, Y.; Chen, L.; Bao, W.; Ren, Y.; Gao, Y.; Yin, Y.; Zhao, Y. Glycine-mediated, selective preparation of monodisperse spherical vaterite calcium carbonate in various reaction systems. *Cryst. Growth Des.* **2015**, *15*, 1194–1200. [[CrossRef](#)]
55. Warren, B.E.; Bisce, J. The structure of silica glass by X-ray diffraction studies. *J. Am. Ceram. Soc.* **2010**, *21*.
56. Andersen, F.A.; Brecevic, L. Infrared spectra of amorphous and crystalline calcium carbonate. *Acta Chem. Scand* **1991**, *45*, 1018–1024. [[CrossRef](#)]
57. Reig, F.B.; Adelaar, J.G.; Moreno, M.M. FTIR quantitative analysis of calcium carbonate (calcite) and silica (quartz) mixtures using the constant ratio method. Application to geological samples. *Talanta* **2002**, *4*, 811–821. [[CrossRef](#)]
58. Wolf, G.; Königsberger, E.; Schmidt, H.G.; Königsberger, L.C.; Gamsjäger, H. Thermodynamic aspects of the Vaterite-Calcite Phase Transition. *J. Therm. Anal. Calorim.* **2000**, *60*, 463–472. [[CrossRef](#)]
59. Gao, M.; Wang, W.; Yang, H. Hydrothermal synthesis of hierarchical hollow hydroxyapatite microspheres with excellent fluoride adsorption property. *Microporous Mesoporous Mater.* **2019**, *289*, 109620. [[CrossRef](#)]
60. Gholami, T.; Salavati-Niasari, M.; Bazarganipour, M.; Norri, E. Synthesis and characterization of spherical silica nanoparticles by modified Stöber process assisted by organic ligand. *Superlattices Microstruct.* **2013**, *61*, 33–41. [[CrossRef](#)]
61. Pota, G.; Venezia, V.; Vitiello, G. Tuning functional behavior of humic acids through interactions with stober silica nanoparticles. *Polymers* **2020**, *4*, 982. [[CrossRef](#)] [[PubMed](#)]
62. Zhao, T.; Xu, C.; Ma, Y.; Zeng, Y.; Wang, N. Study on preparation and structure of chrysanthemum-shaped micron calcium carbonate based on inverse microemulsion. *Micro Nano Lett.* **2020**, *3*, 1–5. [[CrossRef](#)]
63. Sun, J.; Hwang, J.Y.; Jankowski, P.; Xiao, L.; Sanchez, J.S.; Xia, Z.; Lee, S.; Talyzin, A.V.; Matic, A.; Palermo, V.; et al. Critical Role of Functional Groups Containing N, S, and O on Graphene Surface for Stable and Fast Charging Li-S Batteries. *Small* **2021**, *17*, 1–10. [[CrossRef](#)] [[PubMed](#)]
64. Li, X.G.; Lv, Y.; Ma, B.G.; Wang, W.Q.; Jian, S.W. Decomposition kinetic characteristics of calcium carbonate containing organic acids by TGA. *Arab. J. Chem.* **2013**. [[CrossRef](#)]
65. Ding, H.; Shou-Ci, L.U.; Deng, Y.X.; Xiang, D.-G. Mechano-activated surface modification of calcium carbonate in wet stirred mill and its properties. *Trans. Nonferrous Met. Soc. China* **2007**, *17*, 1100–1104. [[CrossRef](#)]

-
66. Sun, J.; Memon, M.A.; Bai, W.; Xiao, L.; Zhang, B.; Jin, Y.; Huang, Y.; Geng, J. Controllable fabrication of transparent macroporous graphene thin films and versatile applications as a conducting platform. *Adv. Funct. Mater.* **2015**, *25*, 4334–4343. [[CrossRef](#)]
 67. Sun, J.; Sadd, M.; Edenborg, P.; Grönbeck, H.; Thiesen, P.H.; Xia, Z.; Quintano, V.; Qiu, R.; Matic, A.; Palermo, V. Real-time imaging of Na⁺ reversible intercalation in “Janus” graphene stacks for battery applications. *Sci. Adv.* **2021**, *7*, 1–11. [[CrossRef](#)]